Black Phosphorus–Graphene Heterostructure-Supported Pd Nanoparticles with Superior Activity and Stability for Ethanol Electro-oxidation

Tong Wu,[†] Yu Ma,[‡,§] Zhibei Qu,[‡] Jinchen Fan,*,[†,‡,∥] Qiaoxia Li,[†,∥] Penghui Shi,[†,∥] Qunjie Xu,*,[†,∥] and Yulin Min*,[†,∥]

[†]Shanghai Key Laboratory of Materials Protection and Advanced Materials in Electric Power, College of Environmental and Chemical Engineering, Shanghai University of Electric Power, Shanghai 200090, P. R. China

[‡]Department of Chemical Engineering and Biointerfaces Institute, University of Michigan, Ann Arbor, Michigan 48109, United States

[§]School of Physical Science and Technology, Lanzhou University, Lanzhou 730000, P. R. China

[∥]Shanghai Institute of Pollution Control and Ecological Security, Shanghai 200092, P. R. China

* Supporting Information

ABSTRACT: Rational design supporting material for palladium (Pd)-based catalyst can maximize its electrocatalytic performance for ethanol oxidation reaction (EOR) catalyst in alkaline condition. Utilizing the unique two-dimensional structures and outstanding physicochemical property of graphene and black phosphorus (BP), herein, we proposed and designed a black phosphorus−graphene heterostructure for supporting Pd nanoparticles. Through merely ball-milling of activated graphene (AG) and black phosphorus (BP), the AG−BP hybrid with a linkage of P−C bonding is used as supports of Pd. The obtained Pd/AG−BP hybrid exhibits ultrahigh electrochemical activity toward EOR. Remarkably, it can achieve a high mass peak current density of $\sim$6004.53 and $\sim$712.03 mA mg$_{Pd}^{-1}$ before and after the durability tests of 20 000s on EOR, which are $\sim$7.19 and 80 times higher than those of commercial Pd/C. The experimental analysis and density-functional-theory calculation show that Pd becomes more positive with electrons transfer from Pd to AG−BP supports and is liable to absorb the OH radicals for removing CO$_{ads}$ intermediate to release active sites on EOR, together with the excellent ability to generate additional OH militants after combining with the AG−BP heterostructure.

KEYWORDS: palladium, graphene, black phosphorus, catalysts, ethanol electro-oxidation
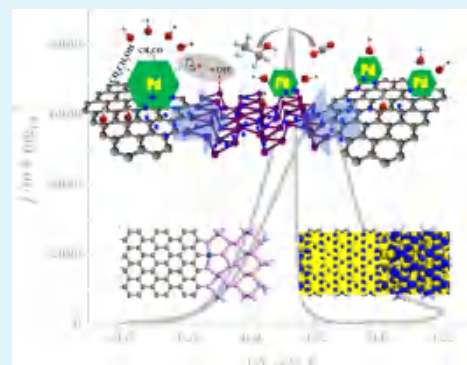
1. INTRODUCTION

Fuel cell research and development have always been one of the critical topics in renewable, green energy resources due to the expeditious consumption of limited fossil fuels. Direct ethanol fuel cells (DEFCs) are almost recognized as the good choices for next-generation power supplier because ethanol is a plentiful and low-cost liquid fuel that can be easily prepared from biomass. Electrocatalyst plays an essential role in the system of DEFCs. Good electrocatalyst can provide a high reaction efficiency and rate, even benign selectivity of the chemical transformations toward ethanol oxidation reaction (EOR). Among the currently available EOR catalysts, Pd-based catalysts only have much lower production cost but also exhibit higher EOR activity in alkaline media than Pt-based catalysts.[1−4] Nevertheless, the stability and lifetime for Pd-based catalysts toward EOR remain critical issues. In the meantime, the complete oxidation of ethanol still is the challenge for designing high-performance Pd-based catalysts. Seh et al.[5] concluded that exposing more active sites on

catalysts and improving intrinsic activity are the primary ways to improve the performance (or reaction rate) of an electrocatalyst. Therefore, designing excellent Pd-based catalysts toward EOR is vital to enhance the electroactivity and stability (sometimes, selectivity). Up to now, combining with other metals such as Ru, Au, or Ir, Sn, or Cu to construct Pd−M binary or ternary catalysts and preparing Pd-based hybrids with the introduction of supports (carbon-based materials, metal oxides, and conducting polymers) were always considered as effective ways to further improve the EOR activities of Pd catalysts.[6−8] Supported catalysts with good catalyst supports can not only reduce the usage amount of Pd but also are conducive to expose more surface-active sites probably because of their high conductivity, large surface area, and high dispersion of Pd.[9,10]
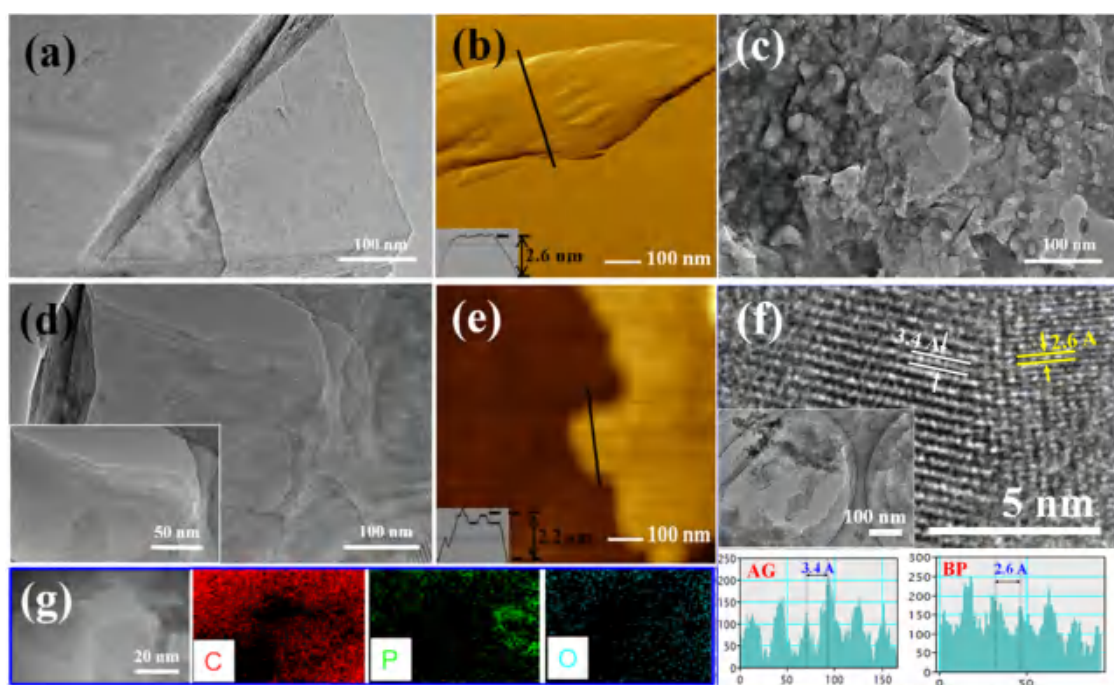
Figure 1. (a) Typical TEM image of CPG, (b) AFM image of CPG, (c) TEM image of AG, (d) TEM image of BP nanoflakes, (e) AFM image of BP nanoflakes, (f) High-resolution transmission electron microscopy (HRTEM) image of AG−BP, and (g) energy-dispersive spectroscopy (EDS) mapping images for C, P, and O elements in AG−BP.

Graphene, a fascinating two-dimensional (2D) nanomaterial, has been widely considered as a favorable catalyst support due to its large surface area and high electroconductivity.[11] Zhao et al.[12] prepared the polypyrrole-functionalized graphene (PPy-graphene) as supports for Pd nanoparticles (NPs). The Pd/PPy-graphene shows higher electrocatalytic performances than Pd/Vulcan for methanol oxidation. Guo et al.[13] used graphene to support ultrasmall palladium (Pd) nanocrystals for improving the electrocatalytic performance of formic acid oxidation. Chen et al.[14] developed a surfactant-free method for combining graphene oxide (GO) with Pd NPs. The resulting Pd NPs-GO shows high electrocatalytic ability in EOR. Based on the above analysis, it is not hard to conclude that the single introduction of graphene has a positive action for better growth and dispersion of Pd NPs to enhance the final EOR activity. However, reviewing the mechanism of Pd-based catalysts toward EOR, the removal of reaction intermediates, e.g., CO, can further improve the electrochemically active area (ECSA) of Pd and then promote the catalytic activity significantly. Chen et al.[15] used the density functional theory (DFT) calculation to show that the combination between the intermediates of *OH and *CH$_3$CO is the rate-determining step. The *CH$_3$CO solely decomposes into *CO and *CH$_3$ in the poisoning-intermediate pathway, which blocks the active site and deteriorates the efficacy of the catalysts. In the context of the catalyst system with facile, the generation of *OH intermediates and high CO tolerance are beneficial to improve the electrocatalytic performance toward EOR. In other words, *OH can promote the oxidation of carbonaceous poison intermediates on Pd active sites and thereby facilitate the selectivity accompanied by improvement in catalyst stability.[15]

In back Pd/graphene EOR catalysts, modifying the electronic band structure of graphene with doping heteroatoms (e.g., N, S, P, etc.) and introducing transition-metal oxides (MnO$_2$, CeO$_2$, TiO$_2$, etc.) into the Pd/graphene EOR catalysts are highly effective ways for enhancing the electrocatalytic activity by promoting the generation of addition *OH in alkaline. Black phosphorus (BP) has attracted significant interest due to its high carrier mobility, considerable on/off ratio, and the band gap ranging from 0.3 to 1 eV, depending on its thickness.[16−21] The BP monolayer has exceptionally high hole mobility.[19−22] It is worth noting that BP has a strong affinity to water and can serve as excellent sites for water dissociative adsorption. In our previous work, we found that the introduction of hole-conductive 2D BP can facilitate the generation of *OH and stripping of reactive intermediates.[23]

On the basis of the above analysis, we proposed a novel approach to rational fabricate graphene−BP heterostructure for supporting Pd to improve the EOR activity. Herein, BP was combined with the structure of potassium hydroxide (KOH)-activated graphene (AG) to prepare a novel graphene−BP heterostructure support of Pd NPs through merely ball-milling of AG and BP. The results demonstrated that the Pd/AG−BP hybrid exhibits ultrahigh electrochemical activity toward EOR in alkaline condition. The AG−BP heterostructure with a linkage of a P−C bond can facilitate the generation of addition OH species (OH$_{ads}$) for the oxidation of carbonaceous poison intermediates. Further, the DFT calculations were also conducted to evaluate the electrocatalytic performance toward EOR from a theoretical aspect.

2. RESULTS AND DISCUSSION

2.1. Morphologies and Structures of Pd/AG−BP Hybrids. Commercial pristine graphene (CPG) nanosheets used in this study were obtained by mechanical exfoliation of graphite. As shown in Figure 1a, the CPG is transparent under the electron beam, indicating that CPG is flat and thin enough. The thickness of the CPG was determined by atomic force microscopy (AFM). Figure 1b shows that an isolated CPG with the thickness of ∼2.6 nm contains about eight layers of
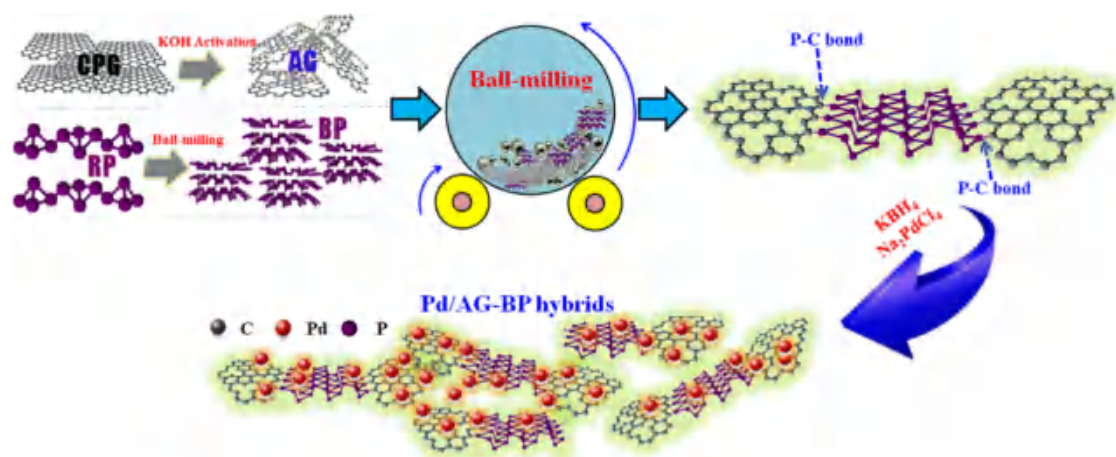
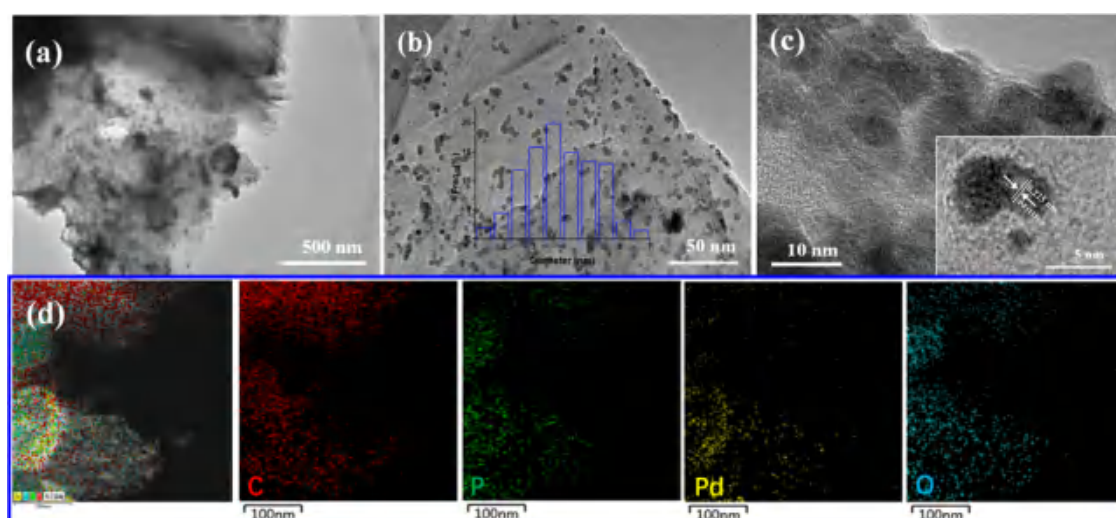Figure 2. Schematic diagram for the preparation of Pd/AG−BP catalysts.

Figure 3. (a) TEM image of Pd/AG−BP hybrids, (b) TEM image of the Pd/AG−BP hybrids and size distribution histogram of Pd NPs, (c) HRTEM images of the Pd/AG−BP hybrids, and (d) EDS mapping images for C, P, Pd, and O elements in Pd/AG−BP.

single-layer graphene. For the fabrication of heterostructure of graphene nanosheets and black phosphorous (BP), the CPG were first chemically activated by KOH. After activation, the Brunauer−Emmett−Teller (BET) surface area sharply increased from 24.6 for CPG to 620.06 m^2 g^{-1} for the as-prepared activated CPG (AG) (Figure S1a). The resulting AG shows a visible mesoporous structure and its pore size is between 10 and 40 nm (Figure S1b). There are lots of holes in the structure of the as-prepared AG nanoflakes, as shown in the transmission electron microscopy (TEM) image (Figure 1c). The defects and holes induced by KOH activation are conducive to further combination with BP nanoflakes. The BP nanoflakes were obtained by high-energy ball-milling red phosphorous, which is reported by Park et al.[24] Figure 1d shows the typical TEM image of BP nanoflakes with an apparent layered structure. A close examination of the edge of a piece of BP nanoflakes shows about five layers of phosphorene. From the AFM image (Figure 1e), the thickness of an individual BP nanoflake is determined to be ~2.2 nm.

As shown in Figure 2, the AG−BP heterostructure (AG−BP) was facile prepared by direct ball-milling of AG and BP under the protection of argon. Like previous black phosphorus−graphite composites reported by Sun et al., the

robust phosphorus−carbon (P−C) bonds between BP nano-flakes and AG can be generated in the ball-milling process. The AG−BP heterostructure is linked by robust P−C bonds. The energy-dispersive spectroscopy (EDS) demonstrated that the elements of C, P, and O are uniformly distributed in the AG−BP heterostructure. The thickness of AG−BP is about 45.302 nm, which is much higher than that of AG (~2.6 nm) and BP (~2.2 nm) (Figure S2a,b). It may be because BP and AG are stacked together by covalent P−C bonds in the vertical dimension. The inset TEM image of Figure 1f shows that the porous structure of AG almost disappeared. This may be due to that the porous structure of AG is filled by BP through the covalent bond between AG and BP. The BET surface area of AG−BP is ~37.8 m^2 g^{-1}, which is much less than that of AG (620.06 m^2 g^{-1}), implying that the porous structure of AG has changed dramatically (Figure S3a). From the Barret−Joyner−Halenda (BJH) pore size distribution, the peak intensities in the range of 20−40 nm are close to zero, which is lower than that of AG (Figure S3b). It gives the evidence that the porous structure of AG has changed, and the holes of AG are filled with and covered by BP nanoflakes with P−C linkages. As shown in Figure 1f, there is a distinct boundary of AG and BP in the AG−BP heterostructure. It has two parallel dark lines in
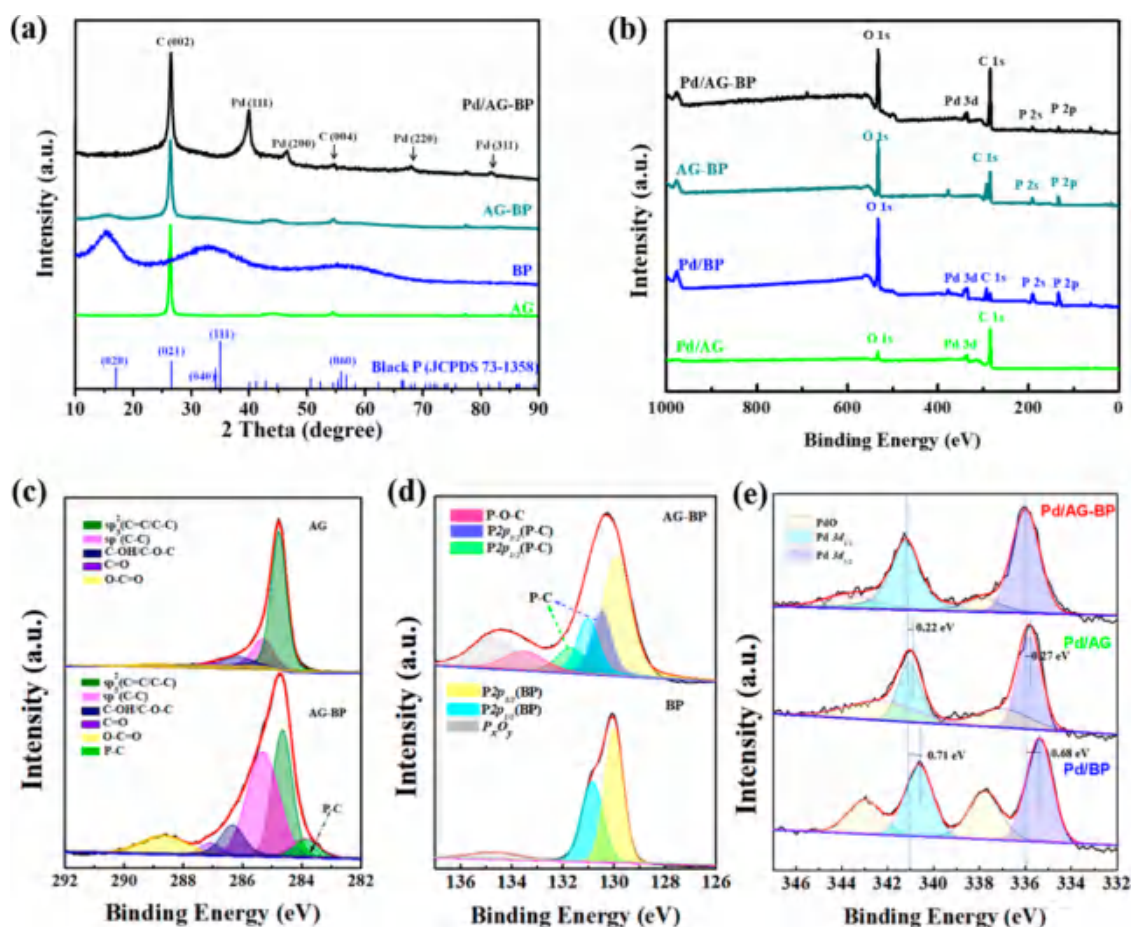
Figure 4. (a) XRD patterns of Pd/AG−BP, AG−BP, BP, and AG, (b) X-ray photoelectron spectroscopy (XPS) survey of Pd/AG, Pd/BP, AG−BP, and Pd/AG−BP, and high-resolution region of (c) C 1s for AG and AG−BP, (d) P 2p for BP and AG−BP, and Pd 3d (e) for Pd/BP, Pd/AG, and Pd/AG−BP.

different directions with different interplanar spacing. The lattice distance of 0.34 nm is ascribed to the C (002) plane the interplanar spacing of AG. The lattice distance of 0.26 nm corresponded to the (040) faces of BP.

Using Na_2PdCl_4 and KBH_4 as a precursor and a reductant, respectively, the Pd/AG−BP catalysts with different Pd loading amounts were prepared. From the TEM images of Pd/AG−BP catalysts (Figure 3a,b), the Pd NPs are homogeneously distributed on the AG−BP heterostructure. Statistical analysis shows that the mean size of Pd NPs is ∼3.7 nm. High-resolution transmission electron microscopy (HRTEM) image of the Pd/AG−BP clearly shows close contact between Pd NPs and surfaces of AG−BP. From the inset of Figure 3c, the interplanar spacing of 0.225 nm belongs to the (111) planes of face-centered cubic (fcc) Pd. The EDS mapping images provide the visual information on the distribution of elements in Pd/AG−BP catalysts. From the EDS mapping image (Figure 3d), the C and O elements are well distributed in the selected area of Pd/AG−BP catalysts. The element P mainly abound below the selected area, distinguished from element C, supporting the formation of the AG−BP heterostructure with distinct boundaries between BP and AG. Notably, from the EDS image, the Pd NPs is apt to grow and anchor on the BP region of the AG−BP. It is maybe ascribed to more active surfaces of BP with the existence of phosphoric oxides (P_xO_y) than that of AG. From the X-ray diffraction (XRD) patterns (Figure 4a), there is a diffraction peak at 25.6° in AG, which is

attributed to the C (002) plane diffractions. The characteristic peaks at 2θ = 15, 33.5, and 55.6° are assigned to BP, which fits the standard pattern of orthorhombic black P (JCPDS no. 73-1358).[25] Regarding the Pd/AG−BP hybrids, the peaks at 2θ = 40.1, 46.7, 68.1, and 82.1° are indexed to the (111), (200), (220), and (311) crystalline planes of the fcc Pd, respectively.[26] The personal reflections of BP became weaker in AG−BP and Pd/AG−BP hybrids due to the generation of P−C bond and formation of P_xO_y.

X-ray photoelectron spectroscopy (XPS) was also performed on Pd/AG−BP to examine the electronic structure and surface information. The characteristic peaks of C 1s, P 2s, P 2p, and O 1s appeared in the XPS spectrum of Pd/AG−BP (Figure 4b). Ball-milling BP and AG generated the P−C bonds under an Ar atmosphere. Lots of defects were induced by KOH activation in the structure of AG, which is conducive to the coupling of AG and BP. Using XPS-peak-differentiation-imitating analysis (Figure 4c), the peak located at ∼283.5 eV in the C 1s survey of AG−BP demonstrated the formation of the P−C bond. The P 2p XPS spectra of BP (Figure 4d) was fitted to the P $2p_{1/2}$ (130.85 eV) and P $2p_{3/2}$ (129.9 eV) doublet, which is split by ∼0.85 eV. Toward the P 2p XPS spectra of AG−BP, apart from the P $2p_{1/2}$ and P $2p_{3/2}$ peaks from the P−P bond of BP, the peaks at 130.46 and 131.68 eV are ascribed to the P $2p_{1/2}$ and P $2p_{3/2}$ doublet from the generated P−C bond. The formation of robust P−C bonds provides different interfaces between BP and AG, leading to
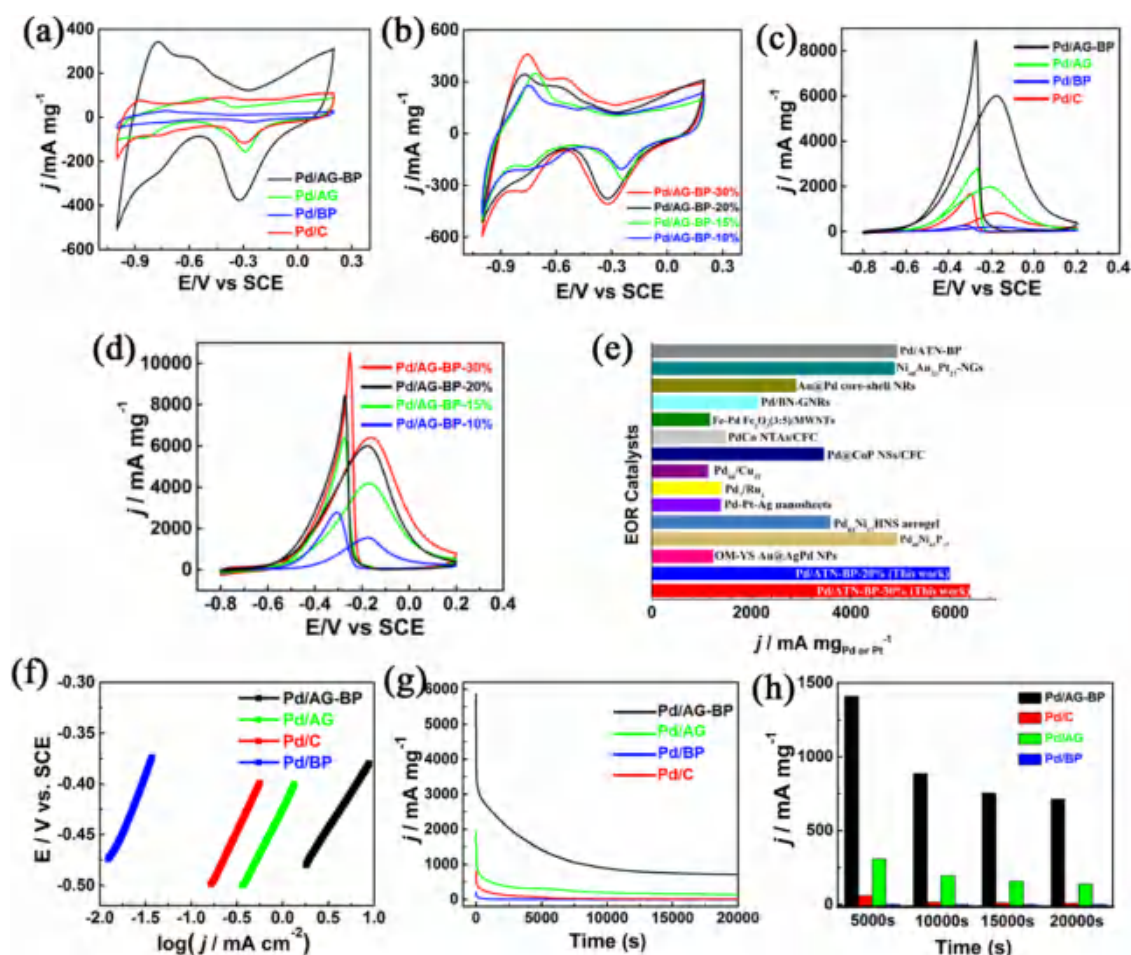
Figure 5. (a) CVs of the Pd-based catalysts with different supports in a 1.0 M sodium hydroxide solution (scan rate: 50 mV s^{-1}), (b) CVs for the Pd/AG−BP catalysts in a 1.0 M sodium hydroxide solution (scan rate: 50 mV s^{-1}), (c) CVs for the Pd-based catalysts with different supports in a 1.0 M sodium hydroxide and 1.0 M ethanol mixture solution (scan rate: 50 mV s^{-1}), (d) CVs of Pd/AG−BP catalysts with different contents of Pd in 1.0 M sodium hydroxide solution (scan rate: 5 0 mV s^{-1}), (e) comparison of mass activities for recent EOR catalysts, (f) Tafel plots of the catalysts, (g) chronoamperometric curves for the Pd-based catalysts with different supports, and (h) the current densities of the catalysts toward EOR after durability tests of different times.

improvement in the structural stability of AG−BP. The heterostructure of AG−BP in the Pd/G−BP catalysts affords surprisingly a high performance and stability on the EOR activity in an alkaline condition. The XPS spectra of Pd/G−BP and Pd/BP in the Pd 3d regions were analyzed to explore the effect of the AG−BP heterostructure. As can be seen from Figure 4e, the partial Pd exists as PdO status in all the catalysts, especially in the Pd/BP catalyst. It is generally recognized that the defects of BP produced by ball-milling can generate unsaturated active sites. Then, the Pd ion can be easily reduced to Pd atom on the AG−BP heterostructure, with defects induced from ball-milling.[27] From the peak areas, the contents of PdO in Pd/AG−BP is lower than those of Pd/AG and Pd/BP. Moreover, the Pd 3d$_{3/2}$ and Pd 3d$_{5/2}$ peaks of Pd/AG−BP both shift to 341.25 and 335.95 eV, respectively. Compared with those of Pd/BP, there are positive shifts (ca. 0.71 and 0.68 eV) for Pd 3d$_{3/2}$ and Pd 3d$_{5/2}$ peaks in binding energies, which are related to the strong electron interactions between Pd and carbon atoms. Also, the binding energies of Pd 3d$_{3/2}$ and Pd 3d$_{5/2}$ peaks for Pd/AG−BP are also higher than those for Pd/AG. The positive shifts (ca. 0.22 and 0.27 eV) confirm the strong electronic interactions between P and Pd in the structure of Pd/AG−BP. The electronic interactions between the three

elements of Pd, P, and C will visibly alter the electronic states of Pd atoms. The electrons are liable to transfer from Pd atoms to the AG−BP supports with AG combined with p-type BP. The positive shifts of the Pd characteristic peaks in binding energy imply that the core level of Pd shifts down with respect to the Fermi level. Evidently, the strong electronic interactions between Pd and AG−BP leads to a downshift of the d-band center of Pd.[28] It makes Pd more positive together with the enhancement of both the binding energy and the electrocatalytic activity and stability of Pd/AG−BP.

2.2. Electrocatalytic Performances. Using AG−BP for supporting Pd NPs, the obtained Pd/AG−BP hybrids were used as electrocatalysts in EOR. Cyclic voltammograms (CVs) were first performed in N$_2$-saturated sodium hydroxide solution (1 mol L^{-1}) at a scan rate of 50 mV s^{-1} to evaluate their electrochemical performance. As shown in Figure 5a, there are distinct current peaks from −1.0 to −0.6 V in CV curves for all Pd-based catalysts with different supports. These peaks originated from the hydrogen adsorption/desorption behavior on Pd sites. The mass current densities of the hydrogen adsorption/desorption peaks are much higher than those of Pd/C, Pd/AG, and Pd/BP. At around −0.30 V vs saturated calomel electrode (SCE), the Pd/AG−BP also shows
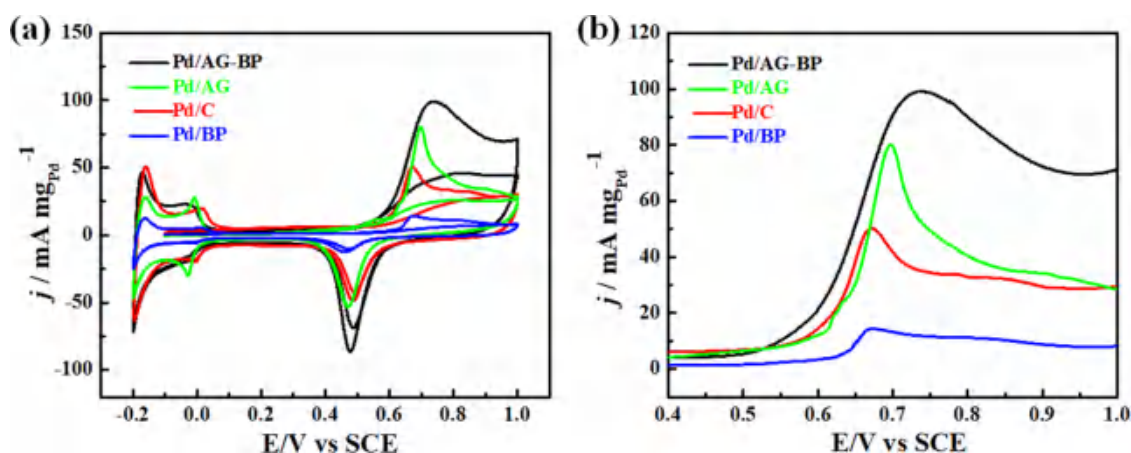
Figure 6. (a) CVs for CO stripping of the catalysts and (b) CO monolayer stripping voltammograms of the catalysts. Condition: 0.5 M sulfuric acid solution and scan rate: 10 mV s^{-1}.

the highest reduction peak. The electrochemically active area (ECSA)$_{PdO}$ can be estimated by determining the Coulombic charge involved in the reduction of a PdO monolayer.[23] The ECSA$_{PdO}$ of Pd/AG, Pd/BP, and commercial Pd/C catalysts are 103.75, 20.62, and 59.64 m^2 g$_{Pd}^{-1}$, respectively. In comparison, Pd/AG−BP shows the highest ECSA$_{PdO}$ of 276.98 m^2 g$_{Pd}^{-1}$, which is 2.67, 13.43, and 4.64 times higher than that of Pd/AG, Pd/BP, and commercial Pd/C. Figure 5b shows the CV curves of Pd/AG−BP catalysts with different percentages of Pd. The compositions of Pd were determined from inductively coupled plasma atomic emission spectroscopy (ICP-AES) (Table S1). With increase in the Pd loading amount, the ECSA$_{PdO}$ of Pd/AG−BP increases from 92.05 m^2 g$_{Pd}^{-1}$ for Pd/AG−BP-10% (Pd: 3.82 wt %) to 336.81 m^2 g$_{Pd}^{-1}$ for Pd/AG−BP-30% (Pd: 16.55 wt %). The high ECSA$_{PdO}$ of Pd/AG−BP demonstrates that more catalytic active sites of Pd are exposed after combining with the AG−BP heterostructure. Further, the electrocatalytic performances of Pd/AG−BP toward EOR were evaluated in a sodium hydroxide and ethanol mixture solution. From Figure 5c, the peak current densities of Pd/AG, Pd/C, and Pd/BP are 1972, 834.5, and 208.6 mA mg$_{Pd}^{-1}$, respectively. Remarkably, for Pd/AG−BP-20% catalyst, the peak current density is very high and incredibly achieved at 6004.53 mA mg$_{Pd}^{-1}$. It is almost 3.04, 7.19, and 28.78 times higher than those of Pd/AG, Pd/C, and Pd/BP, respectively. For Pd/AG−BP-30% catalyst, the mass peak current density increased to 6410.8 mA mg$_{Pd}^{-1}$ (Figure 5d). From Figure 5e, the mass peak current densities of Pd/AG−BP-20% and Pd/AG−BP-30% catalysts are higher that those of those of the various reported EOR catalysts (Figure 5e).[15,29−40] Figure 5f shows the linear regions of the Tafel plots at a scan rate of 1 mV s^{-1}. The Tafel slopes of Pd/AG, Pd/BP, Pd/C, and Pd/AG−BP catalysts are 176.9, 222.4, 190, and 142.1 mV dec^{-1}, respectively. The Pd/AG−BP (140.4 mV dec^{-1}) shows the lowest Tafel slope. It indicates the fastest charge-transfer kinetics of Pd/AG−BP in the alkaline medium and strong synergistic catalyst−support interactions between Pd NPs and the heterostructure of direct-gap graphene and hole-conductive BP.[41,42]

The durability stability of Pd/AG−BP toward EOR is evaluated by chronoamperometry in a 1.0 M sodium hydroxide and 1.0 M ethanol mixture solution with a constant potential of 0.2 V vs SCE. From Figure 5g,h, the Pd/AG−BP always exhibits the highest current densities among all catalysts at different times. In other words, the Pd/AG−BP catalyst shows the highest electrochemical durability. It is worth noting that there are rapid decreases of current densities at the beginning of durability tests for all catalysts. It is mainly attributed to the formation of the surface oxides on Pd. Even so, the Pd/AG−BP catalyst still exhibits the greatest stability on EOR, with the current density remaining at 712.03 mA mg$_{Pd}^{-1}$ after at 20 000 s, which was 80, 5, and 904 times higher than those for Pd/C, Pd/AG, and Pd/BP, respectively. The retention rates of the peak current density (i$_{20000}$/i$_{5000}$) on Pd/AG−BP-20%, Pd/C, and Pd/AG are 50.5, 14.4, and 45.5%, respectively. On the one hand, the inherent structural stability of AG−BP heterostructure formed by covalent P−C bonding helps improve the durability stability of the Pd/AG−BP catalysts. On the other hand, there are strong synergistic interactions between Pd NPs and AG−BP that facilitate the stripping of reactive intermediates and then improve the tolerance. Further, the peak current ratios of forward to backward scan (j$_f$/j$_b$) were calculated to evaluate the contamination arising from poisoning species.[23] It can be seen from Table S1 that the j$_f$/j$_b$ ratio of the Pd/AG−BP catalyst is higher than that of the commercial Pd/C catalyst. It indicates that the AG−BP support plays a significant role in removing CO$_{ad}$ intermediates on the surfaces of Pd NPs. The antipoisoning tests of the Pd/AG−BP catalyst were further evaluated by CO-stripping voltammograms (Figure 6a,b). The onset potentials for the Pd/AG−BP-30%, Pd/AG, Pd/C, and Pd/BP catalysts were 0.49, 0.52, 0.55, and 0.63 V, respectively. The Pd/AG−BP has a much lower onset potential, indicating the positive role of AG−BP supports in promoting the oxidative removal of CO species. The ECSA related to the CO$_{ad}$ intermediates oxidation (ECSA$_{CO}$) was also calculated and is illustrated in Table S1.[23] The ECSA$_{CO}$ of Pd/AG−BP, Pd/AG, Pd/C, and Pd/BP are 274.3, 192.01, 147.86, and 91.17 m^2 g^{-1}, respectively (Figure 6b). The highest ECSA$_{CO}$ values of Pd/AG−BP imply that more surfaces active area sites are released, which is consistent with the ECSA$_{PdO}$.

Meanwhile, the BP flakes are easily oxidized into P$_x$O$_y$. Regarding the benign water adsorption of P$_x$O$_y$, the concentration of OH species increases on the catalyst surfaces (AG−BP + H$_2$O = AG−BP−(OH)$_{ad}$ + H$^+$ + e$^-$).[23] It is well-known that the reactant OH$_{ad}$ is indispensable for the removal of CO$_{ad}$ intermediates. Thereby, the high concentration of OH$_{ad}$ can facilitate the total oxidation of CO$_{ad}$ to CO$_2$ (AG−
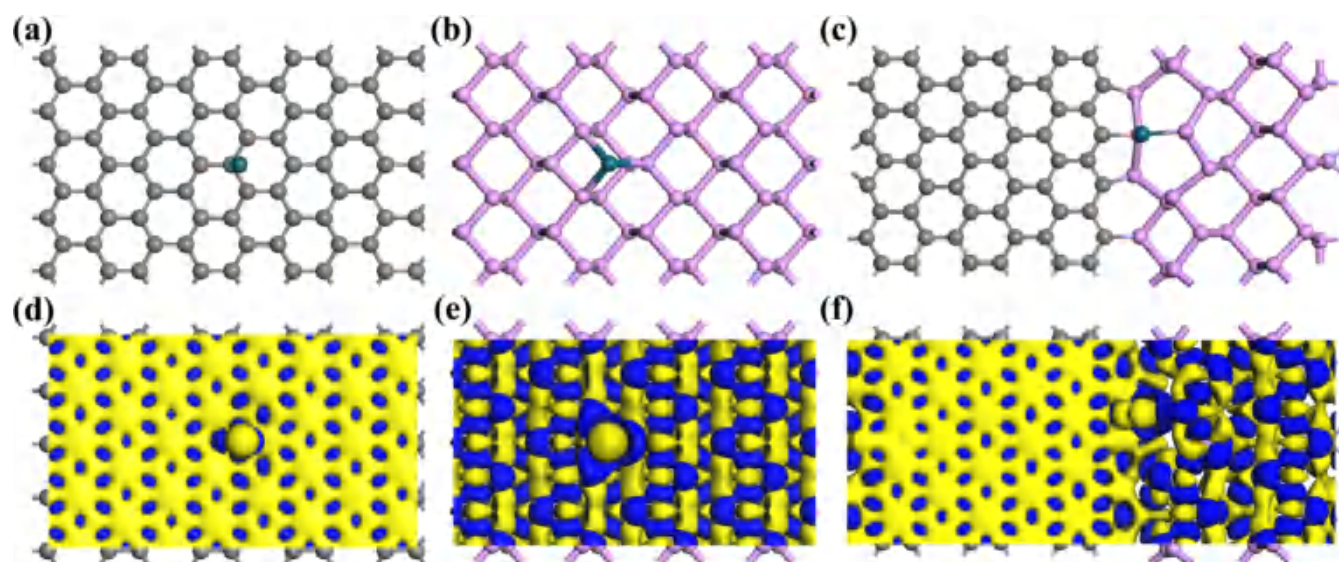
Figure 7. Optimized geometric structures of (a) Pd/AG, (b) Pd/BP, and (c) Pd/AG−BP. Electron density difference isosurfaces for (d) Pd/BP, (e) Pd/AG, and (f) Pd/AG−BP. Gray ball for C atom; Purple ball for P atom; and green ball for Pd atom. Yellow solid for positive density difference and blue solid for negative density difference. The value was set at 0.02 eV.
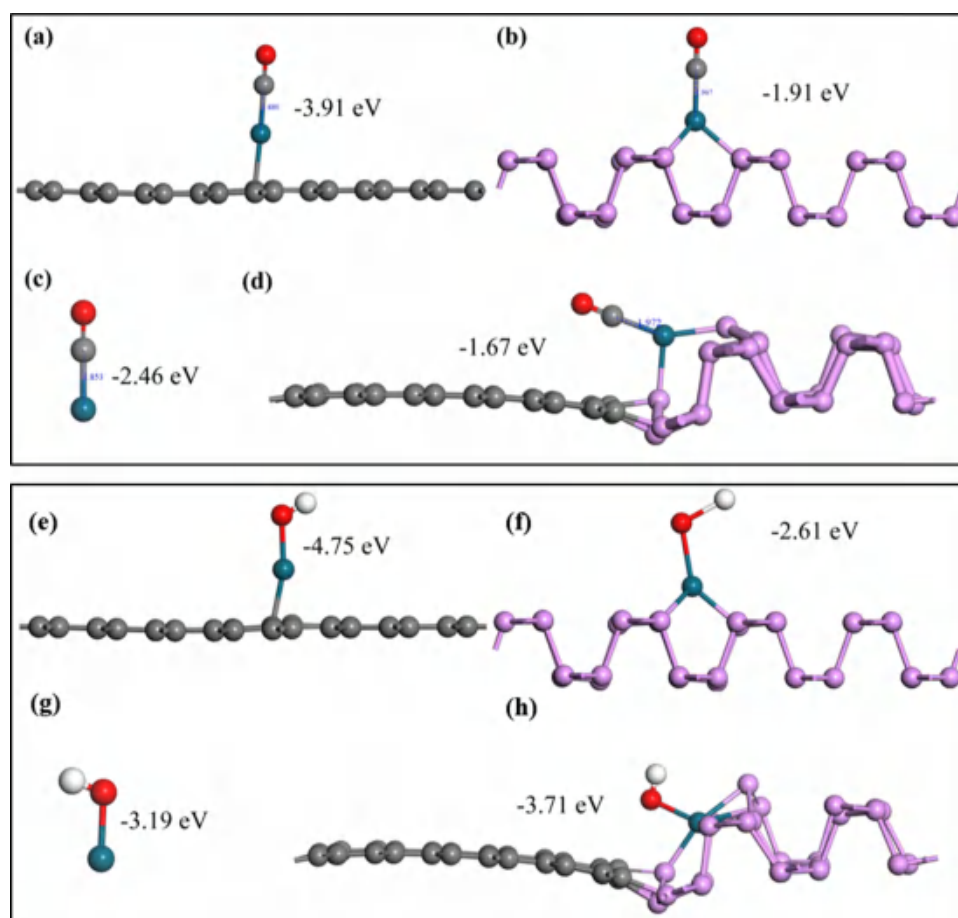

Figure 8. Optimized geometric structures and their CO absorption energies for (a) Pd/AG, (b) Pd/BP, (c) atomic Pd, and (d) Pd/AG−BP. Optimized geometric structures and their hydroxyl absorption energies for (e) Pd/AG, (f) Pd/BP, (g) atomic Pd, and (h) Pd/AG−BP. Gray ball for C atom, Purple ball for P atom, green ball for Pd atom, and Red ball for oxygen.

$BP-(OH)_{ad} + Pd-(CO)_{ad} = AG-BP + Pd + CO_2 + H^+ + e^-)$.[43] As a result, the CO-like intermediate species were oxidized to CO_2, fresh active sites were generated, and finally the anti-CO poisoning ability of the Pd/AG−BP catalysts was improved. The AG−BP heterostructure greatly promotes the generation of OH_{ad}, improves the oxidation and stripping of the reaction intermediates on the surfaces of Pd sites, and

finally leads to the significant increment of ECSA$_{CO}$ for Pd/AG−BP catalyst.[23]

2.3. DFT Calculations. In the EOR reactive-intermediate pathway, the combination of *OH and *CH$_3$CO intermediates has been confirmed as the rate-determining step for EOR.[44] In the poisoning-intermediate pathway, *CO, which is decomposed from *CH$_3$CO intermediate, significantly blocks the active site of Pd and deteriorates the electrochemical activity of the Pd-based catalysts. For the Pd/AG−BP hybrid catalyst, the transfer of electrons from Pd to the supports of AG−BP makes Pd more positive; as a result, the Pd active sites tend to absorb *OH by electrostatic interaction easily. Meantime, the AG−BP supports with facile *OH generation favor excellent electrocatalytic performance toward EOR. To verify the mechanism, we proposed that DFT calculations be performed to evaluate the electrocatalytic performance toward EOR from theoretical point of view. The simplified single-layer graphene and black phosphorus were applied to represent AG and BP supports. A heterojunction model of single-layer graphene and black phosphorus layer was applied to represent AG−BP. The carbon−phosphorus bonds formed in the model were verified by TEM and XPS characterizations. The Pd atom absorption on AG, BP, and AG−BP support is illustrated in Figure 7, together with their electron density difference isosurfaces. All Pd/AG, Pd/BP, and Pd/AG−BP structures show a high electron density difference around the Pd atom. The electron density gain of Pd/AG is relatively small such that the absorption of Pd atom on graphene is relatively weak. The electron density gain of Pd/BP is higher such that strong valence bonds are formed between Pd and BP. For Pd/AG−BP structure, the density gain is even higher such that graphene will donate an electron to BP through the heterojunction. It is known that negative minimum electrostatic potential (MEP) of the surface will weaken CO adsorption. The MEP of the supports was calculated such that Pd/AG−BP shows the smallest MEP of −0.42 eV, whereas the MEPs for Pd/AG and Pd/BP were −0.22 and −0.24 eV, respectively.

The absorption models of CO on Pd/AG, Pd/BP, and Pd/AG−BP structures were calculated (Figure 8a−d). The Pd/AG−BP structure holds the highest absorption energy (−1.67 eV), along with the most extended C−Pd bond length (1.972 Å), corresponding to the MEP results. The high absorption energy means that the CO absorbed on the Pd/AG−BP catalyst will be much easier to desorb, as CO poisoning is the most severe problem that hinders the catalytic performance of Pd-based catalysts toward EOR process. The easy desorption of CO will significantly contribute to the performance improvement of the catalysis. The absorption models of OH radicals on Pd/AG, Pd/BP, and Pd/AG−BP structures were calculated (Figure 8e−h). Differently, the Pd/AG−BP catalyst shows a highly negative absorption energy (−3.71 eV) of OH$_{ads}$. The OH radicals will be more favorable to be absorbed on Pd/AG−BP, which is beneficial for EOR performance.

3. CONCLUSIONS

In summary, we successfully prepared the AG−BP heterostructure for supporting Pd NPs to enhance the activity of EOR catalysts. By simply ball-milling AG and BP, the AG−BP heterostructure linked with stable P−C bonding was successfully obtained. The results demonstrated that Pd NPs are mainly dispersed on the surfaces of the BP region in the AG−BP heterostructure with the mean size of ∼3.7 nm. The

as-prepared Pd/AG−BP hybrid catalysts show ultrahigh electrochemical activity on EOR in alkaline condition. The mass peak current densities of Pd/AG−BP-20% and Pd/AG−BP-30% are 6004.53 and 6410.8 mA mg$_{Pd}^{-1}$, respectively, which are 7.19 and 7.68 times higher than those of Pd/C. Moreover, the Pd/AG−BP catalysts also show very high stability. After a durability test of 20 000 s, there is a retention rate of ≈11.8% for Pd/AG−BP-20%. Based on the experimental analysis and DFT calculation, the support of AG−BP heterostructure makes Pd more positive and easier to absorb OH radicals for removing CO$_{ads}$ intermediate to release active sites on EOR. Also, calculating from the models for desorption of CO and absorption of OH radicals, for Pd/AG−BP catalyst, the CO$_{ads}$ is much easier to desorb and OH radicals are more favorable to be absorbed than that for Pd/AG and Pd/BP. Benefiting from the synergistic interaction between AG−BP and Pd, high-performance EOR activity can be achieved by using the AG−BP heterostructure, which also can act as high-performance support for other noble-metal-based catalysts and greatly improve their electrochemical activities. We also have reasons to believe that the hole-conductive BP can be widely used to rational fabricate BP-based heterostructure in energy-related applications.

4. METHODS

4.1. Reagents and Chemicals. Graphene powder (physical methods, size: 0.5−5 μm, thickness: 1−2 nm, single-layer ratio: ∼80%) was purchased from Nanjing XFNANO Materials Tech Co., Ltd. Red phosphorus (99.999% metals basis, 1−5 mm), sodium tetrachloropalladate (purity 98%), and potassium borohydride (KBH$_4$, purity ≥ 97%) were obtained from Shanghai Aladdin Reagent Co., Ltd. Nafion solution (5 wt %) was purchased from Shanghai Geshi Energy Technology Co., Ltd. Ethanol (AR, ≥99.7%) and cetyltrimethyl ammonium bromide were provided from Sinopharm Chemical Reagent Co., Ltd. The chemicals are all used as obtained without any purification.

4.2. Activation of Commercial Pristine Graphene (CPG) Nanosheets. The CPG was activated by potassium hydroxide (KOH). Briefly, the CPG powder was first soaked in 30 mL of KOH aqueous solution (6 mol L^{-1}) for 12 h. Then, the CPG was filtrated and dried in a vacuum oven at 60 °C overnight. Next, the CPG was further treated at 800 °C for 2 h under an N$_2$ atmosphere. Finally, the activated CPG (AG) was collected after subsequent natural cooling to room temperature.

4.3. Fabrication of AG−BP. BP was prepared by directly ball-milling red phosphorus under an argon (Ar) atmosphere according to the previously reported method.[23,45] For preparing the AG−BP, 200 mg of BP and 200 mg of AG were added into 50 mL stainless steel vacuum grinding jar (the weight ratio of the ball to powder was 60/1; 500 rpm). Then, the argon gas was continuously injected into the stainless steel vacuum grinding jar for 1 h to remove the air and prevent the degradation of black phosphorus. After ball-milling of 48 h, the AG−BP hybrids were collected and stored in a sealed bottle filled with argon gas.

4.4. Preparation of Pd/AG−BP. Twenty milligrams of AG−BP was first added into 20 mL of ethanol. After dispersion with 1 h of sonication, a certain amount of Na$_2$PdCl$_4$ was added to the above dispersion. Adjusting the pH value of the mixture dispersion to 10.0 with 1 M sodium hydroxide, 10 mL of KBH$_4$/ethanol solution (0.2 mol L^{-1}) was slowly added to the above mixture dispersion with a miniature peristaltic pump. Next, the mixture dispersion was reacted for 12 h at room temperature under magnetic stirring. Afterward, the Pd/AG−BP was collected from the reacted mixture dispersion by filtration. After washing with water and ethanol twice, the obtained Pd/AG−BP was dried at 50 °C in vacuum oven for 12 h. The Pd/AG, Pd/BP, and Pd/C were also prepared by the same process for comparison. The weight ratios of Pd in the Pd/AG-BP were

controlled by the feed mass percentage of the Pd from Na_2PdCl_4 precursor relative to the catalysts.

4.5. Instruments and Characterization. TEM images were obtained by a JEOL JEM-2100F. XRD characterization was carried out on a Bruker D8-advance X-ray powder diffractometer. XPS measurements were run on a Thermo Scientific ESCALAB 250Xi with Al $K\alpha$ X-ray (1486.8 eV) radiation. Inductively coupled plasma optical emission spectrometry (ICP-OES) was carried out by Agilent 720 Axial ICP-OES. Atomic force microscopy (AFM) measurements were conducted in an Agilent 5500AFM with tapping mode. The N_2 adsorption−desorption isotherms and pore size were determined using a Micromeritics ASAP 2010 analyzer.

4.6. Electrocatalytic Measurement. The electrochemical activities of all catalysts were tested using three-electrode systems on a CHI660E electrochemical workstation. The platinum foil (1.0 × 1.0 cm^2) and saturated calomel electrode (SCE) were used as the counter and reference electrodes, respectively. A glassy carbon rotating disk electrode (Φ = 3 mm) with a casting thin layer of Nafion impregnated catalyst was used as the working electrode (Pd loading: 28 μg cm^{-2}). The CV curves of the catalysts were obtained in 1.0 M sodium hydroxide solution at room temperature with the potential range from −1.0 to 0.2 V vs SCE. The catalytic activities of the catalysts were studied in a sodium hydroxide and ethanol mixture solution. The experiments for CO stripping were conducted in a 0.5 M sulfuric acid solution. Before the experiments, all the electrolytes were bubbled with nitrogen gas for 1 h.

■ ASSOCIATED CONTENT

* Supporting Information

The Supporting Information is available free of charge on the ACS Publications website at DOI: 10.1021/acsami.8b20240.

> Results of all catalysts used in the EOR; nitrogen adsorption/desorption isotherms and Barret−Joyner− Halenda (BJH) pore size distributions of CPG and AG; AFM images of AG−BP; nitrogen adsorption/desorption isotherms and Barret−Joyner−Halenda (BJH) pore size distribution of AG−BP; optimized geometric structures for AG and BP; optimized geometric structures for AG−BP-1, AG−BP-2, Pd/AG, and Pd/ BP; optimized geometric structures and their absorption energies for various absorption sites of Pd atom on AG− BP and optimized geometric structures and their hydroxyl absorption energies for Pd/AG, Pd/BP, atomic Pd, and Pd/AG−BP (PDF)

■ AUTHOR INFORMATION

Corresponding Authors
*E-mail: Jinchen.fan@shiep.edu.cn (J.F.).
*E-mail: xuqunjie@shiep.edu.cn (Q.X.).
*E-mail: minyulin@shiep.edu.cn (Y.M.).
ORCID ⊙
Jinchen Fan: 0000-0002-8905-1693
Notes
The authors declare no competing financial interest.

■ ACKNOWLEDGMENTS

■ REFERENCES

(1) Jiang, K.; Wang, P.; Guo, S.; Zhang, X.; Shen, X.; Lu, G.; Su, D.; Huang, X. Ordered PdCu-Based Nanoparticles as Bifunctional Oxygen-Reduction and Ethanol-Oxidation Electrocatalysts. Angew. Chem., Int. Ed. 2016, 128, 9176−9181.

(2) Xu, C.; Liu, Y.; Yuan, D. Pt and Pd Supported on Carbon Microspheres for Alcohol Electrooxidation in Alkaline Media. Int. J. Electrochem. Sci. 2007, 2, 674−680.

(3) Wang, W.; Jing, W.; Sheng, L.; Chai, D.; Kang, Y.; Lei, Z. Pd$_3$Cu Coupling with Nitrogen-doped Mesoporous Carbon to Boost Performance in Glycerol Oxidation. Appl. Catal., A 2017, 538, 123−130.

(4) Wang, W.; Dong, Y.; Xu, L.; Dong, W.; Niu, X.; Lei, Z. Combining Bimetallic-Alloy with Selenium Functionalized Carbon to Enhance Electrocatalytic Activity towards Glucose Oxidation. Electrochim. Acta 2017, 244, 16−25.

(5) Seh, Z. W.; Kibsgaard, J.; Dickens, C. F.; Chorkendorff, I.; Nørskov, J. K.; Jaramillo, T. F. Combining Theory and Experiment in Electrocatalysis: Insights into Materials Design. Science 2017, 355, No. eaad4998.

(6) Mavrokefalos, C. K.; Hasan, M.; Khunsin, W.; Schmidt, M.; Maier, S. A.; Rohan, J. F.; Compton, R. G.; Foord, J. S. Electrochemically Modified Boron-doped Diamond Electrode with Pd and Pd-Sn Nanoparticles for Ethanol Electrooxidation. Electrochim. Acta. 2017, 243, 310−319.

(7) Raja, R.; Hermans, S.; Shephard, D. S.; Johnson, B. F. G.; Raja, R.; Sankar, G.; Bromley, S.; Thomas, J. M. Preparation and Characterisation of A Highly Active Bimetallic (Pd−Ru) Nanoparticle Heterogeneous Catalyst. Chem. Commun. 1999, 16, 1571−1572.

(8) Rikkinen, E.; Santasaloaarnio, A.; Airaksinen, S.; Borghei, M.; Viitanen, V.; Sainio, J.; Kauppinen, E. I.; Kallio, T.; Krause, A. O. I. Atomic Layer Deposition Preparation of Pd Nanoparticles on a Porous Carbon Support for Alcohol Oxidation. J. Phys. Chem. C 2011, 115, 23067−23073.

(9) Bianchini, C.; Shen, P. K. Palladium-based Electrocatalysts for Alcohol Oxidation in Half Cells and in Direct Alcohol Fuel Cells. Chem. Rev. 2009, 109, 4183−4206.

(10) Wang, W.; Jing, W.; Wang, F.; Liu, S.; Liu, X.; Lei, Z. Amorphous Ultra-dispersed Pt Clusters Supported on Nitrogen Functionalized Carbon: A superior Electrocatalyst for Glycerol Electrooxidation. J. Power Sources 2018, 399, 357−362.

(11) Geim, A. K. Graphene: Status and Prospects. Science 2009, 324, 1530−1534.

(12) Zhao, Y.; Lu, Z.; Tian, J.; Nie, S.; Zhen, N. Enhanced Electrocatalytic Oxidation of Methanol on Pd/polypyrrole−graphene in Alkaline Medium. Electrochim. Acta 2011, 56, 1967−1972.

(13) Guo, C. X.; Zhang, L. Y.; Miao, J.; Zhang, J.; Li, C. M. DNA-Functionalized Graphene to Guide Growth of Highly Active Pd Nanocrystals as Efficient Electrocatalyst for Direct Formic Acid Fuel Cells. Adv. Energy Mater. 2013, 3, 167−171.

(14) Chen, X.; Wu, G.; Chen, J.; Chen, X.; Xie, Z.; Wang, X. Synthesis of "Clean" and Well-Dispersive Pd Nanoparticles with Excellent Electrocatalytic Property on Graphene Oxide. J. Am. Chem. Soc. 2011, 133, 3693−3695.

(15) Chen, L.; Lu, L.; Zhu, H.; Chen, Y.; Huang, Y.; Li, Y.; Wang, L. Improved Ethanol Electrooxidation Performance by Shortening Pd− Ni Active Site Distance in Pd−Ni−P Nanocatalysts. Nat. Commun. 2017, 8, No. 14136.

(16) Churchill, H. O. H.; Jarilloherrero, P. Two-dimensional crystals: Phosphorus Joins the Family. Nat. Nanotechnol. 2014, 9, 330−331.

(17) Das, S.; Zhang, W.; Demarteau, M.; Hoffmann, A.; Dubey, M.; Roelofs, A. Tunable Transport Gap in Phosphorene. Nano Lett. 2014, 14, 5733−5739.

(18) Li, L.; Yu, Y.; Ye, G. J.; Ge, Q.; Ou, X.; Wu, H.; Feng, D.; Chen, X. H.; Zhang, Y. Black Phosphorus Field-effect Transistors. Nat. Nanotechnol. 2014, 9, 372−377.

(19) Tran, V.; Soklaski, R.; Liang, Y.; Yang, L. Layer-controlled Band Gap and Anisotropic Excitons in Few-Layer Black Phosphorus. Phys. Rev. B 2014, 89, 817−824.

(20) Viti, L.; Hu, J.; Coquillat, D.; Knap, W.; Tredicucci, A.; Politano, A.; Vitiello, M. S. Black Phosphorus Terahertz Photodetectors. Adv. Mater. 2015, 27, 5567−5572.

(21) Yuan, H.; Liu, X.; Afshinmanesh, F.; Li, W.; Xu, G.; Sun, J.; Lian, B.; Curto, A. G.; Ye, G.; Hikita, Y.; et al. Polarization-sensitive Broadband Photodetector Using a Black Phosphorus Vertical p−n Junction. Nat. Nanotechnol. 2015, 10, 707−713.

(22) Qiao, J.; Kong, X.; Hu, Z. X.; Yang, F.; Ji, W. High-mobility Transport Anisotropy and Linear Dichroism in Few-layer Black Phosphorus. Nat. Commun. 2014, 5, No. 4475.

(23) Wu, T.; Fan, J.; Li, Q.; Shi, P.; Xu, Q.; Min, Y. Palladium Nanoparticles Anchored on Anatase Titanium Dioxide-Black Phosphorus Hybrids with Heterointerfaces: Highly Electroactive and Durable Catalysts for Ethanol Electrooxidation. Adv. Energy Mater. 2018, 8, No. 1701799.

(24) Park, C. M.; Sohn, H. J. Black Phosphorus and Its Composite for Lithium Rechargeable Batteries. ChemInform 2007, 38, 2465−2468.

(25) Shen, Z.; Sun, S.; Wang, W.; Liu, J.; Liu, Z.; Yu, J. A black-red Phosphorus Heterostructure for Efficient Visible-light-driven Photocatalysis. J. Mater. Chem. A 2015, 3, 3285−3288.

(26) Zhou, D.; Ding, L.; Cui, H.; An, H.; Zhai, J.; Li, Q. Fabrication of Pd/TiO$_2$-multiwall Carbon Nanotubes Catalyst and Investigation of Its Electrocatalytic Activity for Formic Acid Oxidation. J. Power Sources 2013, 222, 510−517.

(27) Wang, J.; Liu, D.; Huang, H.; Yang, N.; Yu, B.; Wen, M.; Wang, X.; Chu, P. K.; Yu, X.-F. In-Plane Black Phosphorus/Dicobalt Phosphide Heterostructure for Efficient Electrocatalysis. Angew. Chem., Int. Ed. 2018, 130, 2630−2634.

(28) Wang, J.; Ye, H.; Song, Y. In-situ Reaction-growth of PtNiX Nanocrystals on Supports for Enhanced Electrochemical Catalytic Oxidation of Ethanol via Continuous Flow Microfluidic Process. Electrochim. Acta. 2018, 278, 149−155.

(29) Dutta, A.; Ouyang, J. Ternary NiAuPt Nanoparticles on Reduced Graphene Oxide as Catalysts toward the Electrochemical Oxidation Reaction of Ethanol. ACS Catal. 2015, 5, 1371−1380.

(30) Chen, Y.; Fan, Z.; Luo, Z.; Liu, X.; Lai, Z.; Li, B.; Zong, Y.; Gu, L.; Zhang, H. High-Yield Synthesis of Crystal-Phase-Heterostructured 4H/fcc Au@Pd Core-Shell Nanorods for Electrocatalytic Ethanol Oxidation. Adv. Mater. 2017, 29, No. 1701331.

(31) Liu, Q.; Fan, J.; Min, Y.; Wu, T.; Lin, Y.; Xu, Q. B, N-codoped Graphene Nanoribbons Supported Pd Nanoparticles for Ethanol Electrooxidation Enhancement. J. Mater. Chem. A 2016, 4, 4929−4933.

(32) Wang, Y.; He, Q.; Jiang, G.; Wang, J.; Luo, Z.; Shen, T. D.; Ding, K.; Khasanov, A.; Wei, S.; Guo, Z. Ultrafine FePd Nanoalloys Decorated Multiwalled Cabon Nanotubes toward Enhanced Ethanol Oxidation Reaction. ACS Appl. Mater. Interfaces 2015, 7, 23920−23931.

(33) Wang, A. L.; He, X. J.; Lu, X. F.; Xu, H.; Tong, Y. X.; Li, G. R. Palladium-cobalt Nanotube Arrays Supported on Carbon Fiber Cloth as High-performance Flexible Electrocatalysts for Ethanol Oxidation. Angew. Chem., Int. Ed. 2015, 54, 3669−3673.

(34) Ye, S. H.; Feng, J. X.; Li, G. R. Pd Nanoparticle/CoP Nanosheet Hybrids: Highly Electroactive and Durable Catalysts for Ethanol Electrooxidation. ACS Catal. 2016, 6, 7962−7969.

(35) Zhu, C.; Shi, Q.; Fu, S.; Song, J.; Xia, H.; Du, D.; Lin, Y. Efficient Synthesis of MCu (M = Pd, Pt, and Au) Aerogels with Accelerated Gelation Kinetics and their High Electrocatalytic Activity. Adv. Mater. 2016, 28, 8779−8783.

(36) Zhang, K.; Bin, D.; Yang, B.; Wang, C.; Ren, F.; Du, Y. Ru-assisted Synthesis of Pd/Ru nanodendrites with High Activity for Ethanol Electrooxidation. Nanoscale 2015, 7, 12445−12451.

(37) Hong, J. W.; Kim, Y.; Wi, D. H.; Lee, S.; Lee, S. U.; Lee, Y. W.; Choi, S. I.; Han, S. W. Ultrathin Free-Standing Ternary-Alloy Nanosheets. Angew. Chem., Int. Ed. 2016, 55, 2753−2758.

(38) Cai, B.; Wen, D.; Liu, W.; Herrmann, A. K.; Benad, A.; Eychmüller, A. Function-Led Design of Aerogels: Self-Assembly of Alloyed PdNi Hollow Nanospheres for Efficient Electrocatalysis. Angew. Chem., Int. Ed. 2015, 54, 13101−13105.

(39) Shi, Q.; Zhang, P.; Li, Y.; Xia, H.; Wang, D.; Tao, X. Synthesis of Open-mouthed, Yolk-shell Au@AgPd Nanoparticles with Access to Interior Surfaces for Enhanced Electrocatalysis. Chem. Sci. 2015, 6, 4350−4357.

(40) Huang, W.; Ma, X. Y.; Han, W.; Feng, R.; Zhou, J.; Duchesne, P. N.; Peng, Z.; Chen, F.; Na, H.; Zhao, F.; et al. Promoting Effect of Ni(OH)$_2$ on Palladium Nanocrystals Leads to Greatly Improved Operation Durability for Electrocatalytic Ethanol Oxidation in Alkaline Solution. Adv. Mater. 2017, 29, No. 1703057.

(41) Du, W.; Mackenzie, K. E.; Milano, D. F.; Deskins, N. A.; Dong, S.; Teng, X. Palladium−Tin Alloyed Catalysts for the Ethanol Oxidation Reaction in an Alkaline Medium. ACS Catal. 2012, 2, 287−297.

(42) Du, W.; Wang, Q.; Saxner, D.; Deskins, N. A.; Su, D.; Krzanowski, J. E.; Frenkel, A. I.; Teng, X. Highly Active Iridium/Iridium−Tin/Tin Oxide Heterogeneous Nanoparticles as Alternative Electrocatalysts for the Ethanol Oxidation Reaction. J. Am. Chem. Soc. 2011, 133, 15172−15183.

(43) Pech-Rodríguez, W. J.; González-Quijano, D.; Vargas-Gutiérrez, G.; Morais, C.; Napporn, T. W.; Rodríguez-Varela, F. J. Electrochemical and in situ FTIR Study of the Ethanol Oxidation Reaction on PtMo/C Nanomaterials in Alkaline media. Appl. Catal., B 2017, 203, 654−662.

(44) Jin, C.; Wan, C.; Dong, R. High Activity of Pd Deposited on Ag/C for Allyl Alcohol Oxidation. Electrochim. Acta 2018, 262, 319−325.

(45) Sun, L.-Q.; Li, M.-J.; Sun, K.; Yu, S.-H.; Wang, R.-S.; Xie, H.-M. Electrochemical Activity of Black Phosphorus as an Anode Material for Lithium-Ion Batteries. J. Phys. Chem. C 2012, 116, 14772−14779.